SCIENCE CHINA
Physics, Mechanics & Astronomy

December 2022 Vol. 65 No. 12: 129704
https://doi.org/10.1007/s11433-022-2033-2

• Article •
Special Topic: Peering into the Milky Way by FAST

arXiv:2211.11302v2 [astro-ph.GA] 30 Nov 2022

Peering into the Milky Way by FAST: III. Magnetic fields in the Galactic halo and farther spiral arms revealed by the Faraday effect of faint pulsars

Jun Xu [1*], JinLin Han[1,2*], PengFei Wang[1,2], and Yi Yan[1,2]

[1] *National Astronomical Observatories, Chinese Academy of Sciences, Beijing 100101, China;*
[2] *School of Astronomy, University of Chinese Academy of Sciences, Beijing 100049, China*

Received July 14, 2022; accepted November 10, 2022; published online November 23, 2022

The Five-hundred-meter Aperture Spherical radio Telescope (FAST) is the most sensitive radio telescope for pulsar observations. We make polarimetric measurements of a large number of faint and distant pulsars using the FAST. We present the new measurements of Faraday rotation for 134 faint pulsars in the Galactic halo. Significant improvements are also made for some basic pulsar parameters for 15 of them. We analyse the newly determined rotation measures (RMs) for the Galactic magnetic fields by using these 134 halo pulsars, together with previously available RMs for pulsars and extragalactic radio sources and also the newly determined RMs for another 311 faint pulsars which are either newly discovered in the project of the Galactic Plane Pulsar Snapshot (GPPS) survey or previously known pulsars without RMs. The RM tomographic analysis in the first Galactic quadrant gives roughly the same field strength of around 2 μG for the large-scale toroidal halo magnetic fields. The scale height of the halo magnetic fields is found to be at least 2.7±0.3 kpc. The RM differentiation of a large number of pulsars in the Galactic disk in the Galactic longitude range of $26^\circ < l < 90^\circ$ gives evidence for the clockwise magnetic fields (viewed from the north Galactic pole) in two interarm regions inside the Scutum arm and between the Scutum and Sagittarius arm, and the clockwise fields in the Local-Perseus interarm region and field reversals in the Perseus arm and beyond.

Key Words: magnetic fields, interstellar medium, pulsars

PACS number(s): 95.85.Sz, 98.38.-j, 97.60.Gb

Citation: J. Xu, J. L. Han, P. F. Wang, Y. Yan, Peering into the Milky Way by FAST: III. Magnetic fields in the Galactic halo and farther spiral arms revealed by the Faraday effect of faint pulsars, Sci. China-Phys. Mech. Astron. **65**, 129704 (2022), https://doi.org/10.1007/s11433-022-2033-2

1 Introduction

The Five-hundred-meter Aperture Spherical radio Telescope (FAST, Nan, 2008; Nan et al., 2011), mounted with the 19-beam L-band receiver, is an extremely sensitive radio telescope to observe pulsars and spectral lines for HI gas and ionised gas. The Galactic Plane Pulsar Snapshot (GPPS) survey[1)] is to search for pulsars in the FAST accessible sky within $|b| \leq 10^\circ$ (Han et al., 2021). During the GPPS survey observations, the piggyback spectral data are simultaneously recorded with 1024 K channels for the band of 1000 – 1500 MHz. This series of papers are dedicated to the investigations of the interstellar medium by FAST. The first paper of this series by Hong et al. (2022) is on the exquisite HI struc-

1) Corresponding authors (Jun Xu email: xujun@nao.cas.cn; JinLin Han email: hjl@nao.cas.cn)
1) http://zmtt.bao.ac.cn/GPPS/

© Science China Press and Springer-Verlag GmbH Germany, part of Springer Nature 2020

tures from the high resolution and high sensitivity piggyback HI line observations of the FAST GPPS survey. The second paper of this series by Hou et al. (2022) is on the piggyback recombination line observations of the FAST GPPS survey for HII regions and interstellar ionised gas. This is the third paper on the interstellar magnetic fields revealed by measuring Faraday effect of large number of weak pulsars, for which the polarization properties are difficult to measure without FAST. The fourth paper of this series by Gao et al. (2022) is using the FAST 19-beam L-band receiver of the FAST to scan a sky area of $5^\circ \times 7^\circ$ to get the image of radio continuum emission and identify two large nearby supernova remnants G203.1+6.6 and G206.7+6.0, one of which is very close to our Sun.

Magnetic fields are ubiquitous in galaxies and play crucial roles in astrophysics and astroparticle physics. For example, the magnetic fields affect the evolution of molecular clouds and star formation (see reviews e.g. Crutcher, 2012) and are agents for transport of cosmic rays (e.g. Letessier-Selvon & Stanev, 2011; Prouza & Šmída, 2003) and propagation of axionlike particles (e.g. Xiao et al., 2021). However, many aspects of the Galactic magnetic fields are unknown because the fields have merely been measured for some components in limited regions (see a review by Han, 2017). It is very challenging to reveal the global magnetic structure of the Milky Way Galaxy since we live inside at nearly the edge of the disk.

Several tracers for interstellar magnetic fields have been largely observed, including starlight polarization (e.g. Clemens et al., 2012; Heiles, 1996), polarized thermal emission from aligned dust grains in molecular clouds (e.g. Planck Collaboration et al., 2016b), synchrotron emission from the diffuse interstellar medium (ISM) (e.g. Bennett et al., 2013; Planck Collaboration et al., 2016a), Zeeman splitting of spectral lines from clouds or clumps (e.g. Crutcher et al., 2010), and Faraday rotation of polarized radio sources (e.g. Simard-Normandin & Kronberg, 1980; Taylor et al., 2009). Generally, these tracers only give information for one component of the magnetic fields either parallel or perpendicular to the line of sight.

Faraday rotation of linearly polarized emission from pulsars and extragalactic radio sources (EGRS) is an excellent probe for magnetic fields in our Galaxy (Han, 2017). Pulsars are often highly polarized and have negligible intrinsic Faraday rotation (Wang et al., 2011). They are widely spread throughout the Galaxy at approximately known distances, allowing three-dimensional tomographic mapping of the field structure. The rotation measure (RM) of a pulsar is an integrated quantity of the product of the electron density and magnetic field strength from a pulsar to us, i.e.

$$\mathrm{RM} = 0.812 \int_0^D n_e \mathbf{B} \cdot \mathrm{d}\mathbf{l}, \tag{1}$$

where n_e is the electron density in cm^{-3}, $\mathbf{B}$ is the vector magnetic field in μG, D is the distance, and $\mathrm{d}\mathbf{l}$ is the unit vector along the line of sight towards us in parsecs. The integrated electron density along the line of sight can be measured by the dispersion of pulses, by $\mathrm{DM} = \int_0^D n_e \mathrm{d}l$. The magnetic field component parallel to the line of sight can be directly obtained by

$$\langle B_\parallel \rangle = 1.232 \frac{\mathrm{RM}}{\mathrm{DM}} = \frac{\int_0^D n_e \mathbf{B} \cdot \mathrm{d}\mathbf{l}}{\int_0^D n_e \, \mathrm{d}l}, \tag{2}$$

where $B_\parallel$ is in μG, RM and DM are in their usual units (rad m^{-2} and cm^{-3} pc). When RMs of a large number of pulsars have been measured, the mean field strength between a pair of pulsars at distances D_1 and D_2 in a given direction can be obtained by

$$\langle B_\parallel \rangle_{D_2 - D_1} = 1.232 \frac{\mathrm{RM}_2 - \mathrm{RM}_1}{\mathrm{DM}_2 - \mathrm{DM}_1}. \tag{3}$$

The reliability of such estimates due to the possible coupling of electron density with a magnetic field in the interstellar medium was questioned by Beck et al. (2003), but has been clarified by detailed simulations by Wu et al. (2015, 2009) for the diffuse ISM with different Mach numbers. On Galactic scales, $\langle B_\parallel \rangle = 1.232\mathrm{RM/DM}$ provides a good estimate of the magnetic field along the line of sight (Seta & Federrath, 2021).

The large-scale Galactic magnetic fields consist of the halo and disc components. The halo fields exist obviously as demonstrated by bright synchrotron sky at low frequencies (e.g. Beuermann et al., 1985). Since we live close to the edge of the Galactic disk, the Galactic halo should be most observable in the mid-latitude regions towards the inner Galaxy. Faraday rotation of a large number of EGRS behind the Galactic halo provides a powerful tool to measure the magnetic fields in the halo. The antisymmetric RM distribution of EGRS in the inner Galaxy found by Han et al. (1997, 1999) suggests that the halo fields are probably bi-toroidal with opposite directions above and below the Galactic plane. Such antisymmetry of the RM sky has been confirmed by more and more RM data from large radio continuum surveys (e.g. Schnitzeler et al., 2019; Taylor et al., 2009) and collections of published RMs (e.g. Hutschenreuter et al., 2022; Oppermann et al., 2012, 2015; Xu & Han, 2014). Based on limited knowledge of reversed bi-toroidal fields in the Galactic halo, the global field models have been proposed and developed over the years (e.g. Jansson & Farrar, 2012; Prouza

& Šmída, 2003; Pshirkov et al., 2011; Sun et al., 2008; Terral & Ferrière, 2017; Xu & Han, 2019). Analysis of pulsar RMs suggests the scale height of the Galactic halo magnetic field is at least 2.0 kpc (Sobey et al., 2019) and local halo field strength should be more than 1.6 μG (Xu & Han, 2019). Analysis of EGRS RMs towards the outer Galaxy indicates different field strengths in the halo above and below the Galactic plane (Mao et al., 2012). There also may exist local vertical magnetic fields (e.g. Han & Qiao, 1994; Mao et al., 2010).

In the Galactic disk, RMs of pulsars and EGRS have revealed several field reversals between the spiral arms. Early studies of 38 pulsar RMs observed by Manchester (1974) show that the local regular magnetic field with a strength of around 2 μG is directed toward $l \sim 90°$, i.e., clockwise when viewed from the north Galactic pole. Later more RMs of pulsars and EGRs support a reversal in the inner Galaxy at or near the Carina-Sagittarius arm (e.g. Chi & Wolfendale, 1990; Lyne & Smith, 1989; Rand & Kulkarni, 1989; Simard-Normandin & Kronberg, 1980; Thomson & Nelson, 1980). Moreover, a second reversal (clockwise) in the inner Galaxy beyond the Crux-Scutum arm is proposed (Rand & Lyne, 1994), and a further reversal near the Norma arm is identified by Han et al. (2002, 1999). Evidence for field reversal(s) near or exterior to the Perseus arm towards the anticenter is also presented by Clegg et al. (1992); Han et al. (1999); Lyne & Smith (1989). Han et al. (2006) analyzed a larger sample of pulsar RMs in the tangential regions of spiral arms to give clear evidence for large-scale counterclockwise fields in the spiral arms and reversed fields in the interarm regions. These reversals are supported by independent analysis by Noutsos et al. (2008) and Nota & Katgert (2010). Han et al. (2018) demonstrated large-scale reversals of the field directions between the arms and the interarm regions more clearly by combining newly observed RMs of more pulsars and more EGRS.

Some models have been proposed to fit the RM data, such as the ring model (Rand & Lyne, 1994; Vallée, 2005), the axisymmetric spiral model (Vallee, 1991) and bisymmetric spiral model (Han et al., 1999; Han & Qiao, 1994; Indrani & Deshpande, 1999), but it is hard to fit just one model for all RM data (Men et al., 2008). The large-scale magnetic fields in the Galactic disk may have a more complex pattern as envisioned (e.g. Ma et al., 2020; Ordog et al., 2017; Shanahan et al., 2019). RMs of EGRS behind the Galactic disk show a strong swing between positive and negative, which can be fitted by the field models with only one or two reversals inside the Solar Circle (e.g. Brown et al., 2007; Jansson & Farrar, 2012; Van Eck et al., 2011, 2021), but cautions should be taken that the integrated RM values over the whole path in the disk from the Galactic outskirts to the Sun are much less sensitive to magnetic field reversals between the arms and the interarm regions along the path.

Currently, 3341 pulsars have been discovered (see Manchester et al., 2005) [2], and 1453 of them have published RMs. Among 1045 pulsars in the Galactic halo ($|b| > 8°$), 472 of them have measured RMs. The remaining unmeasured pulsars are so faint to be measured efficiently by other radio telescopes, except for FAST. Here we present the new measurements of RMs for 134 pulsars using the L-band 19-beam receiver of FAST in two observation projects from 2020 to 2021. Moreover, Wang et al. (2022) have observed a very large sample of pulsars for polarization profiles[3], and determined an additional 311 new RMs for newly-discovered pulsars in the GPPS survey (Han et al., 2021) and distant weak known pulsars in the Galactic longitude range $26° < l < 90°$ towards the inner Galaxy. We use these new measurements, together with previously published pulsar RMs and EGRS RMs, to make tomographic analysis of large-scale magnetic field structure in the Galactic halo and disc. The YMW16 electron density model (Yao et al., 2017) is used to estimate pulsar distances from DMs, which have an uncertainty less than 20 percent for two thirds of pulsars.

The arrangement of our paper is as follows. Our FAST observations and data reduction are described in Section 2. We analyse the magnetic field strength and scale height in the Galactic halo in Section 3, and analyse the magnetic fields in the Galactic disk in Section 4. Finally, the conclusions are given in Section 5.

2 FAST polarization observations for pulsar rotation measures

We observe faint pulsars by using the FAST in the Galactic halo which previously had no measured RMs. The polarization observations were carried out in two projects [PID PT2020_0164 and PID PT2021_0051] with the L-band 19-beam receiver. The first was done between October 2020 to April 2021 towards pulsars with a good position. We track each pulsar by the central beam of the L-band 19-beam receiver for 10 minutes. The second project was carried out between September 2021 to November 2021 for pulsars with large position uncertainties by using the "SnapShotDec" observation mode. This "SnapShotDec" mode is modified from the "snapshot" mode designed for the FAST GPPS survey (Han et al., 2021) but with the reference plane aligned with the Equatorial plane. One snapshot can have 4×19 = 76 adjacent beams in a hexagonal sky region of 28′ wide in declina-

2) http://www.atnf.csiro.au/research/pulsar/psrcat/ (version 1.68)
3) see http://zmtt.bao.ac.cn/psr-fast/

Table 1 Fundamental parameters of 15 pulsars updated by FAST observations

PSR name	Ref.	Period (s)	DM (cm^{-3} pc)	RA(J2000) (hh:mm:ss)	Dec(J2000) (dd:mm:ss)	Items updated	Period(σ) (s)	DM(σ) (cm^{-3} pc)	RA(J2000) (hh:mm:ss)	Dec(J2000) (dd:mm:ss)
(1)	(2)	(3)	(4)	(5)	(6)	(7)	(8)	(9)	(10)	(11)
J0011+08	[1]	2.55287	24.9	00:11:34	+08:10	position	2.552860(18)	25.6(9)	00:11:40	+08:05
J0146+31	[2]	0.9381	25	01:46:15	+31:04	position	0.938067(4)	24.4(5)	01:46:41	+30:55
J0241+16	[3]	1.5454	16	02:41:46	+16:04	position	1.544897(10)	19.3(8)	02:41:22	+16:04
J0244+14	[3]	2.1281	31	02:44:51	+14:27	position	2.127917(12)	29.3(7)	02:45:19	+14:32
J0711+0931	[4],[5]	1.21409	46.238	07:11:36.18	+09:31:25	period	2.428176(8)	46.0(8)	07:11:36.18	+09:31:25
J0806+08	[3]	2.0631	46	08:06:05	+08:17	position	2.063092(20)	48.4(13)	08:06:17	+08:12
J0811+37	[6],[7]	1.2483	16.95	08:11:12	+37:28	position	1.248281(7)	15.9(4)	08:11:19	+37:31
J0827+53	[7]	0.0135	23.103	08:27:48	+53:00	position	0.013526(0)	23.11(2)	08:28:26	+53:04
J0848+16	[3]	0.4524	38	08:48:53	+16:43	position,period	0.904709(2)	38.6(3)	08:48:43	+16:41
J1750+07	[1]	1.90881	55.4	17:50:40	+07:33	period	5.726256(41)	55.6(20)	17:50:40	+07:33
J1802+0128	[8]	0.55426	97.97	18:02:27.45	+01:28:23.7	period	1.108528(2)	97.8(4)	18:02:27.45	+01:28:23.7
J1807+04	[3]	0.7989	53	18:07:25	+04:05	position	0.798766(2)	53.0(3)	18:07:17	+03:59
J1809+17	[7]	2.0667	47.32	18:09:06	+17:04	position	2.066642(12)	46.4(7)	18:09:07	+17:06
J1832+27	[6]	0.6318	46	18:32:10	+27:58	position	0.631707(1)	47.5(2)	18:32:19	+27:49
J1937-00	[3]	0.2401	68.6	19:37:09	–00:17	position	0.2401898(2)	67.98(8)	19:37:03	–00:24

Note: Columns(1)–(6) are names, references, and period, DM, and position in RA(J2000) and Dec(J2000) from the references in Columns(2): [1]: Deneva et al. (2016); [2]: Tyul'bashev et al. (2016); [3]: Deneva et al. (2013); [4]: Lommen et al. (2000); [5]: Bilous et al. (2016); [6]: Tyul'bashev et al. (2017); [7]: Sanidas et al. (2019); [8]: Edwards et al. (2001), and columns (8)-(11) are parameters obtained in our FAST observations. The uncertainty of updated coordinates for columns (10) and (11) is 1′ in total.

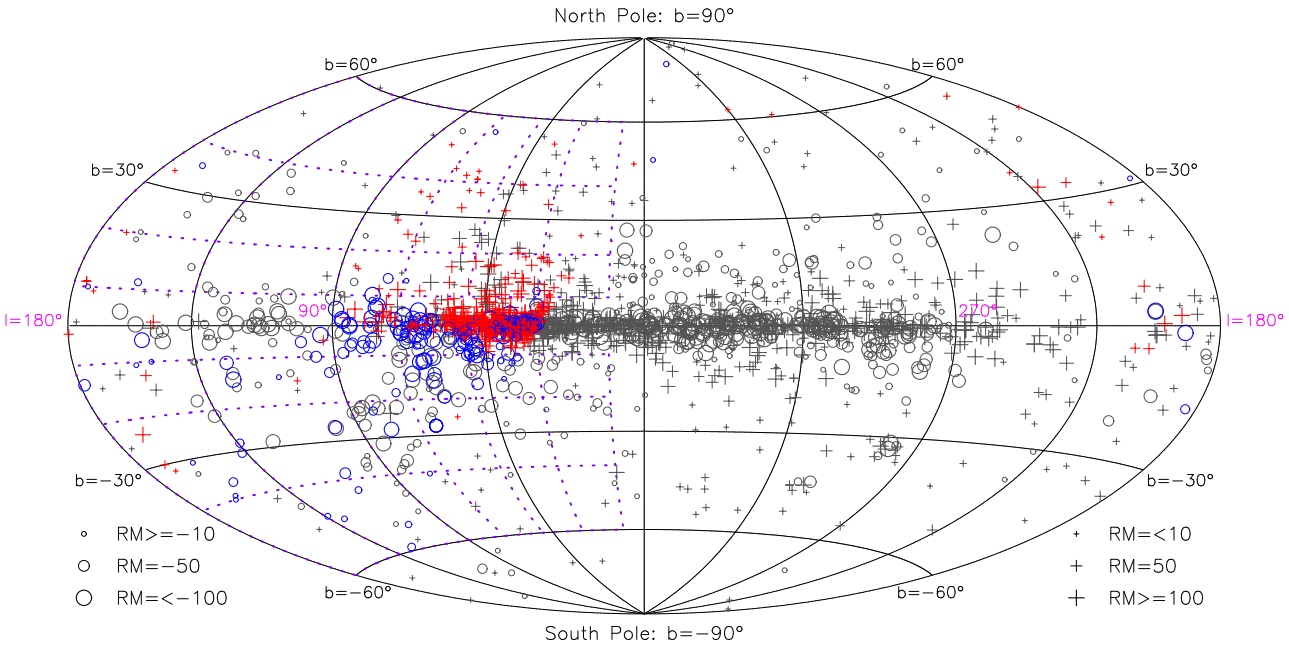


Figure 1 The Galactic distribution of RMs for 1860 pulsars. The sizes of symbols are proportional to the square root of the RM magnitudes, with limits of 10 and 100 rad m^{-2}. The circles and plus signs represent negative and positive RMs, respectively. The red and blue symbols indicate the new measurements of positive and negative RMs from this work and also from the new FAST pulsar database (Wang et al., 2022). Grids divide the sky regions for analysing the magnetic field strength in the Galactic halo in sect. 3.1.

tion. The data of all 19 beams of 4 pointing are all recorded, and the signals of known pulsars are searched from all 76 beams, so that the position of a pulsar can be determined with an uncertainty of 1′ (see Han et al., 2021). The L-band 19-beam receiver is a dual-channel cryogenic system sensitive to orthogonal linear polarization with a system temperature of about 20 – 25 K for different beams (Jiang et al., 2019). The radio signals from the two polarization channels in the frequency range of 1000 to 1500 MHz are amplified, filtered, and then transferred to the digital room via optical fibers. The radio frequency signals are then sampled and channelized to 1024 or 2048 channels in the pulsar digital backend and then composed to 4 polarization for each channel (Han et al., 2021). These data are stored with a sampling time of 49.152 μs in search mode PSRFITS files (Hotan et al., 2004). For each pulsar, a 2-min observation of calibration signals of an amplitude of 10 K or 1 K switching on-off (1 second each) was made on the position, which will be used for system calibration.

Offline data analysis was performed using the PSRCHIVE software package (Hotan et al., 2004). The raw data were first de-dispersed based on the pulsar ephemeris obtained from

Table 2 Rotation measures for 134 halo pulsars

PSR	ObsDate	l (°)	b (°)	Dist* (kpc)	DM* (cm^{-3} pc)	RM (rad m^{-2})	σ
J0006+1834	20210110	108.17	-42.99	0.9	11.41(55)	-19.4	0.4
J0011+08	20210927	106.25	-53.45	5.5	25.6(9)	-17.4	2.7
J0023+0923	20201120	111.38	-52.85	1.8	14.3216(6)	-5.5	3.0
J0050+03	20210117	122.49	-59.07	25.0	26.5(0)	-25.6	2.2
J0058+4950	20201120	124.05	-13.02	2.6	66.953(7)	-114.2	0.5
J0103+54	20210927	124.67	-8.93	2.0	55.605(4)	-74.5	5.4
J0107+1322	20210124	128.99	-49.31	2.3	21.671(1)	-13.9	2.2
J0122+1416	20210110	134.03	-47.94	1.6	17.693(3)	-14.8	4.9
J0139+3336	20210110	134.38	-28.17	1.5	21.23(1)	-29.1	1.1
J0146+31	20210927	136.69	-30.49	1.8	24.4(5)	-32.0	26.6
J0229+20	20210118	151.58	-36.42	2.1	28.5(5)	-32.5	8.7
J0241+16	20210927	157.86	-39.24	0.9	19.3(8)	-6.1	4.2
J0244+14	20210927	159.96	-40.02	2.2	29.3(7)	-8.1	2.1
J0302+2252	20201101	158.44	-30.82	1.0	18.9922(6)	-7.8	0.4
J0329+1654	20201101	168.50	-31.68	2.6	40.821(36)	2.6	4.1
J0337+1715	20201114	169.99	-30.04	1.3	21.3162(3)	26.4	0.1
J0340+4130	20201121	153.78	-11.02	1.6	49.5865(16)	50.5	0.7
J0349+2340	20210427	167.43	-23.38	3.7	62.962(5)	96.6	3.9
J0358+4155	20210108	156.11	-8.62	1.5	46.325(1)	-7.0	0.2
J0453+1559	20210108	184.13	-17.14	0.5	30.3053(3)	-35.2	0.2
J0457+23	20210119	178.31	-12.01	1.5	59(0)	-56.8	0.7
J0518+5416	20210110	155.92	9.56	1.4	42.330(5)	-21.0	10.2
J0605+3757	20210110	174.19	8.02	0.2	20.9462(4)	-0.1	2.7
J0612+37216	20210427	175.44	9.08	1.1	39.270(6)	36.9	1.0
J0613+3731	20210110	175.34	9.24	0.2	18.990(12)	15.3	0.5
J0653+4706	20210130	169.26	19.77	0.9	25.6(1)	12.5	5.3
J0711+0931	20210111	206.67	8.78	1.2	46.0(8)	60.9	0.2
J0806+08	20210928	214.02	20.34	1.9	48.4(13)	10.2	5.0
J0811+37	20210928	183.63	31.25	0.4	15.9(4)	-0.9	1.6
J0813+22	20210928	200.91	27.48	2.4	52.29(5)	14.0	6.6
J0815+4611	20201124	173.63	33.45	0.4	11.2738(3)	2.3	0.4
J0827+53	20210928	165.36	35.74	1.6	23.11(2)	-14.5	3.7
J0848+16	20210928	210.10	33.27	2.4	38.6(3)	38.8	1.6
J0928+06	20210928	226.82	37.56	25.0	49.8(5)	11.0	6.0
J0944+4106	20201124	180.44	49.38	2.7	21.41(3)	1.3	0.8
J1017+3011	20210124	198.43	56.27	25.0	27.150(2)	19.2	0.8
J1038+0032	20201120	247.15	48.47	5.9	26.340(12)	14.3	5.2
J1142+0119	20210427	267.54	59.40	2.2	19.197(1)	-5.2	1.7
J1236-0159	20201219	295.07	60.65	2.0	19.08(3)	1.1	0.7
J1312+0051	20201215	314.84	63.23	1.5	15.345(1)	4.0	0.6
J1312+1810	20210118	332.95	79.76	20.6	25.0(1)	-12.2	1.0
J1501-0046	20201218	356.58	48.05	2.1	22.2584(90)	-1.9	1.0
J1518+0204A	20210111	3.87	46.80	7.5	30.08(5)	2.6	1.9
J1529+40	20210122	66.18	54.91	0.5	6.61(16)	-0.9	0.3
J1538+2345	20201216	37.32	52.39	1.3	14.909(1)	10.6	0.2
J1544+4937	20201219	79.17	50.17	3.0	23.2258(1)	10.3	1.1
J1628+4406	20201026	69.24	43.62	0.5	7.32981(2)	1.6	0.4
J1630+3734	20201216	60.25	43.22	1.2	14.18009(7)	1.1	0.2
J1635+2332	20201026	42.00	39.75	25.0	37.568(6)	25.9	0.8
J1638+4005	20210201	63.77	41.87	25.0	33.417(1)	17.2	3.4
J1641+3627A	20210115	59.00	40.91	7.1	30.4386(5)	10.9	1.7
J1641+3627C	20210115	59.00	40.91	7.1	30.1320(2)	5.9	6.2
J1641+3627D	20210115	59.01	40.91	7.1	30.451(3)	10.7	9.7
J1643+1338	20210203	31.26	34.36	4.6	35.821(1)	36.0	1.0
J1656+00	20211028	19.20	25.47	3.9	46.9(0)	5.1	3.5
J1657+3304	20210203	55.34	37.12	2.4	23.9746(6)	22.2	1.3
J1658+3630	20210203	59.63	37.58	0.2	3.04387(3)	8.2	31.5
J1709+2313	20201027	44.52	32.21	2.2	25.3474(2)	39.1	0.8
J1710+4923	20201013	75.93	36.45	0.5	7.08493(2)	6.9	0.8
J1715+46	20210204	71.86	35.35	1.8	19.82(5)	17.2	0.6
J1722+35	20211030	59.27	32.64	2.2	23.83(6)	35.1	1.5
J1736+05	20210206	29.59	19.21	2.5	42(8)	53.9	1.1
J1738+0333	20201013	27.72	17.74	1.5	33.77312(4)	33.2	0.3
J1738+04	20210206	28.39	18.21	1.1	23.1(6)	26.7	2.8
J1739+0612	20201013	30.26	18.86	25.0	95.4(1)	26.6	0.3
J1741+1351	20201013	37.89	21.64	1.7	24.19871(14)	63.2	3.6
J1743-0339	20201114	21.65	13.40	0.2	30.26(11)	48.2	2.8
J1745-0129	20201129	23.84	14.03	5.5	89.3(3)	36.3	0.9
J1745+1017	20201115	34.87	19.25	1.2	23.9711(3)	24.2	0.3
J1745+1252	20210207	37.38	20.30	11.2	66.141(5)	70.3	3.1
J1750+07	20210208	32.84	16.93	3.8	55.6(20)	54.9	2.7
J1800-0125	20201129	25.75	10.68	1.5	51.0(2)	41.4	0.3
J1800+5034	20201016	78.13	28.44	1.9	22.71(6)	22.3	0.6
J1802+0128	20210117	28.61	11.56	7.7	97.8(4)	18.4	1.1
J1806+1023	20210115	37.31	14.56	3.0	52.03(7)	25.9	0.4
J1806+2819	20210110	54.65	21.67	1.3	18.6802(4)	28.3	8.8
J1807+04	20211123	31.46	11.66	2.4	53.0(3)	92.6	1.3
J1807+0756	20210117	35.15	13.28	7.9	89.29(3)	148.1	1.9
J1809-0119	20210118	26.96	8.63	11.1	138.3(2)	21.7	0.3
J1809+17	20211123	43.89	16.86	3.2	46.4(7)	93.0	0.8
J1810+0705	20210213	34.69	12.25	5.5	79.425(5)	158.3	0.4
J1812+0226	20201129	30.71	9.69	7.2	104.14(3)	-22.7	0.5
J1813+1822	20210116	45.54	16.40	5.0	60.8(5)	116.6	0.4
J1814+1130	20210116	39.21	13.31	4.2	65(1)	64.3	1.9
J1814+22	20210207	49.49	17.78	6.5	62.313(11)	118.5	2.4
J1816+4510	20201230	72.83	24.74	4.4	38.8874(4)	37.6	4.1
J1821+4147	20201031	69.54	22.91	4.4	40.673(3)	35.9	0.4
J1822+1120	20210116	39.87	11.57	7.8	95.2(6)	108.9	1.2
J1828+0625	20210118	36.07	8.02	1.0	22.4331(12)	24.4	1.7
J1829+2456	20210115	53.34	15.61	0.9	13.700(5)	-1.0	0.9
J1832+27	20211123	56.37	16.18	3.7	47.5(2)	61.7	1.8
J1834+10	20210213	40.64	8.61	4.1	78.479(24)	98.2	0.6
J1838+1523	20210117	45.35	9.69	3.5	68.26(3)	160.4	0.4
J1842+1332	20210115	44.05	8.07	6.4	102.5(7)	130.2	0.1
J1843+2024	20210116	50.44	10.85	6.0	85.3(2)	151.9	1.2
J1849+2559	20210427	56.24	11.87	6.1	75.0016(4)	60.1	1.1
J1900+30	20210211	61.76	11.80	6.8	71.8352(22)	127.8	2.2
J1913+3732	20201128	69.10	12.13	7.6	72.3623(41)	-0.4	0.2
J1916+3224	20210212	64.63	9.43	7.9	84.105(2)	55.6	0.8
J1923+4243	20210106	74.72	12.64	4.7	52.99(5)	-40.8	0.2
J1929+3817	20201231	71.17	9.69	9.3	93.4(2)	102.6	0.6
J1933+5335	20210101	85.59	15.77	2.5	33.54(3)	1.2	3.1
J1934+5219	20201219	84.49	15.05	7.7	71.26(15)	7.0	3.1
J1937-00	20211123	37.82	-10.33	3.5	67.98(8)	-15.4	0.8
J1941+4320	20201215	76.85	9.86	6.5	79.361(8)	23.7	1.4
J1947+0915	20210118	47.71	-8.07	5.2	86.5(5)	-114.7	0.2
J1950+05	20210213	44.86	-10.55	3.9	61.5(3)	-59.3	0.7
J1953+1149	20210116	50.71	-8.08	10.5	140.03(3)	-46.1	3.8
J1954+1021	20210117	49.52	-9.00	4.3	81.5(7)	-18.6	0.3
J1954+4357	20210109	78.53	8.17	10.1	130.30(5)	-140.1	0.5
J1957-0002	20210427	40.63	-14.72	1.8	38.443(4)	-8.1	2.6
J2016+1948	20201110	60.52	-8.68	2.2	33.8148(16)	-123.2	0.2
J2017+0603	20201108	48.62	-16.03	1.4	23.92344(9)	-57.4	0.6
J2027+2146	20201111	63.54	-9.59	10.3	97.0915(48)	-211.1	0.8
J2033+1734	20201111	60.86	-13.15	1.7	25.0864(12)	-72.5	0.3
J2040+1657	20201110	61.29	-14.85	4.5	50.6919(14)	-100.9	0.3
J2042+0246	20210111	48.99	-23.02	0.6	9.2694(2)	-25.6	2.8
J2048+2255	20210111	67.45	-12.94	7.6	70.6847(22)	-169.5	0.7
J2051+1248	20210110	59.36	-19.45	4.1	43.45(1)	-68.6	11.5
J2105+07	20210118	57.20	-25.05	25.0	52.6(0)	10.6	0.5
J2122+2426	20210427	73.82	-17.93	0.6	8.500(5)	-28.8	0.2
J2204+2700	20210109	83.00	-22.65	3.2	34.8(11)	-29.8	2.0
J2208+4056	20201018	92.57	-12.11	0.8	11.837(9)	-41.7	0.2
J2209+22	20210129	79.90	-27.79	25.0	45.4(6)	-90.1	0.6
J2227+30	20210126	89.66	-22.82	1.4	19.961(6)	-60.7	2.5
J2229+2643	20201027	87.69	-26.28	1.8	22.7282(4)	-60.0	0.7
J2234+0611	20201020	72.99	-43.01	1.0	10.7670(2)	5.6	3.1
J2234+0944	20201021	76.28	-40.44	1.6	17.8323(2)	-10.4	0.2
J2243+1518	20201109	82.81	-37.38	25.0	39.9(2)	-39.0	1.7
J2302+4442	20201031	103.40	-14.01	0.9	13.788120(0)	17.7	0.2
J2306+31	20210126	97.96	-26.34	25.0	46.13(2)	-79.0	1.1
J2329+4743	20201028	108.96	-12.91	2.4	44.012(2)	-3.9	0.4
J2340+08	20210125	94.82	-50.42	3.3	22.9(1)	-4.7	2.5
J2355+2246	20201101	106.53	-38.32	2.2	23.1(7)	-49.1	1.1

*: The distance and DM value of these pulsars are obtained from the ATNF pulsar catalog (Manchester et al., 2005), and the distances are estimated by using YMW16 model from the DM values.

the ATNF pulsar catalog (Manchester et al., 2005) by using the DSPSR package (van Straten & Bailes, 2011). The ra-

dio frequency interference was examined, and corrupted frequency channels were excised using PAZ and PAZI. The pulsar data were calibrated to compensate for instrumental gain and phase variation across the frequency band according to the calibration files obtained from the two minutes calibration on-off data, and then converted to Stokes parameters. More details and reliability of polarimetric calibration for each beam of the FAST 19-beam receiver can be found in Wang et al. (2022).

Table 3 Comparison of our FAST RMs with published values

PSR name	FAST RM (rad m^{-2})	RM1 or RM2 (rad m^{-2})	Ref
J0006+1834	-19.4 ± 0.4	-20 ± 3	[1]
J0023+0923	-5.5 ± 3.0	-5.1 ± 0.9	[2]*
J0340+4130	50.5 ± 0.7	56.1 ± 0.7	[1]
		53.5 ± 1.1	[3]
J0453+1559	-35.2 ± 0.2	-35 ± 2	[1]
		-35.3 ± 0.3	[2]
J0613+3731	15.3 ± 0.5	16 ± 2	[1]
J0711+0931	60.9 ± 0.2	62.8 ± 1.1	[1]
J1038+0032	14.3 ± 5.2	20 ± 5	[2]*
J1142+0119	-5.2 ± 1.7	0.31 ± 0.11	[2]*
J1312+0051	4.0 ± 0.6	2 ± 1	[2]
J1538+2345	10.6 ± 0.2	11.5 ± 1.1	[1]
J1544+4937	10.3 ± 1.1	9.8 ± 1.9	[1]
J1641+3627A	10.9 ± 1.7	13 ± 3	[1]
J1709+2313	39.1 ± 0.8	37 ± 2	[2]
J1710+4923	6.9 ± 0.8	12 ± 2	[1]
J1736+05	53.9 ± 1.1	44 ± 3	[1]
J1738+0333	33.2 ± 0.3	33 ± 3	[1]
		34.7 ± 0.5	[2]
J1741+1351	63.2 ± 3.6	63.5 ± 0.7	[2]*
J1745+1017	24.2 ± 0.3	27.2 ± 0.3	[2]
J1828+0625	24.4 ± 1.7	20 ± 4	[2]
J1829+2456	-1.0 ± 0.9	0.3 ± 0.6	[2]*
J1834+10	98.2 ± 0.6	97.0 ± 1.7	[1]
J1900+30	127.8 ± 2.2	121 ± 2	[1]*
J2016+1948	-123.2 ± 0.2	-121 ± 4	[1]
J2017+0603	-57.4 ± 0.6	-59 ± 3	[2]
J2027+2146	-211.1 ± 0.8	-210 ± 2	[1]
J2033+1734	-72.5 ± 0.3	-71.5 ± 0.3	[2]
J2040+1657	-100.9 ± 0.3	-98 ± 2	[1]
J2042+0246	-25.6 ± 2.8	-21 ± 2	[2]*
J2208+4056	-41.7 ± 0.2	-40 ± 3	[1]
J2227+30	-60.7 ± 2.5	-58.3 ± 1.9	[1]*
J2229+2643	-60.0 ± 0.7	-61.2 ± 0.3	[2]*
J2234+0611	5.6 ± 3.1	4 ± 1	[2]*
J2234+0944	-10.4 ± 0.2	-11.5 ± 0.5	[2]
J2243+1518	-39.0 ± 1.7	-35.5 ± 0.5	[1]*
J2302+4442	17.7 ± 0.2	19.1 ± 1.6	[1]
		18.4 ± 0.4	[3]
J2340+08	-4.7 ± 2.5	-7 ± 2	[1]*

References. [1]: Ng et al. (2020); [2]: Spiewak et al. (2022); [3]: Wahl et al. (2022); "*" denotes the source for the best value (not from this work).

For the pulsars with large position uncertainties, pulsar search was made first for every beam in a cover of snapshot observation following Han et al. (2021), and then the polarization data of the detection beam are analysed with the same procedures as above. We determined the positions for 12 pulsars, often very bright for FAST, by such beam pointing following the procedure described by Han et al. (2021). Signal-to-noise ratios of pulsar profiles can then be computed for several nearby beams so that the position can be determined according to the positions of beam centers and the signal-to-noise ratios of these nearby beams. The accuracy of the determined position is better than 1′. Our observations also find that the previous period of four pulsars J0711+0931, J0848+16, J1750+07 and J1802+0128 are just harmonics. Their corrected parameters are listed in Table 1.

The rotation measure from the resulting polarization profiles was determined by using RMFIT[4], following Han et al. (2018). First, an initial guess of RM was found by searching for peak linear polarization in the RM range of ±1000 rad m^{-2}. The total linear polarization $L = (Q^2 + U^2)^{1/2}$ was computed by summing across all phase bins and the frequency band after correction of Faraday rotation at each trial RM. Second, the first guess value was iteratively corrected by using the RM-refinement algorithm: integrating the data separately in the two halves of the band by taking the current RM and then obtaining the correction to the RM from computing the weighted differential polarization angle. The uncertainty of RM is calculated from the weighted average uncertainty of position angles in the two halves of the band. Only pulse phase bins with linearly polarized flux which is 3-sigma above the off-pulse in both halves are included in the estimate of differential position angles. The final RM value was then derived by subtracting the ionospheric RM calculated with IonFR[5] (Sotomayor-Beltran et al., 2013). The error in the ionospheric RM was incorporated into the final error of RM value.

We determined rotation measures for 118 pulsars in the first FAST observation project and 16 pulsars in the second, as listed in Table 2. All polarization profiles are published in Wang et al. (2022) as a part of the FAST pulsar database. Figure 1 shows the sky distributions of all halo pulsars together with disk pulsars in the Galactic coordinates. Of the total 134 pulsars, RMs of 36 pulsars were also measured recently by Ng et al. (2020), Spiewak et al. (2022) and Wahl et al. (2022), consistent with our measurements with a smaller uncertainty as listed in Table 3. Marginally significant differences ($> 3\sigma$) are only found for PSRs J0340+4130 (5.6σ), J1142+0119 (3.2σ), J1736+05 (3.1σ), and J1745+1017 (7.1σ), probably due to slightly underestimated uncertainties of some measurements or ionospheric RM corrections.

4) http://psrchive.sourceforge.net/manuals/rmfit
5) https://sourceforge.net/projects/ionfarrot

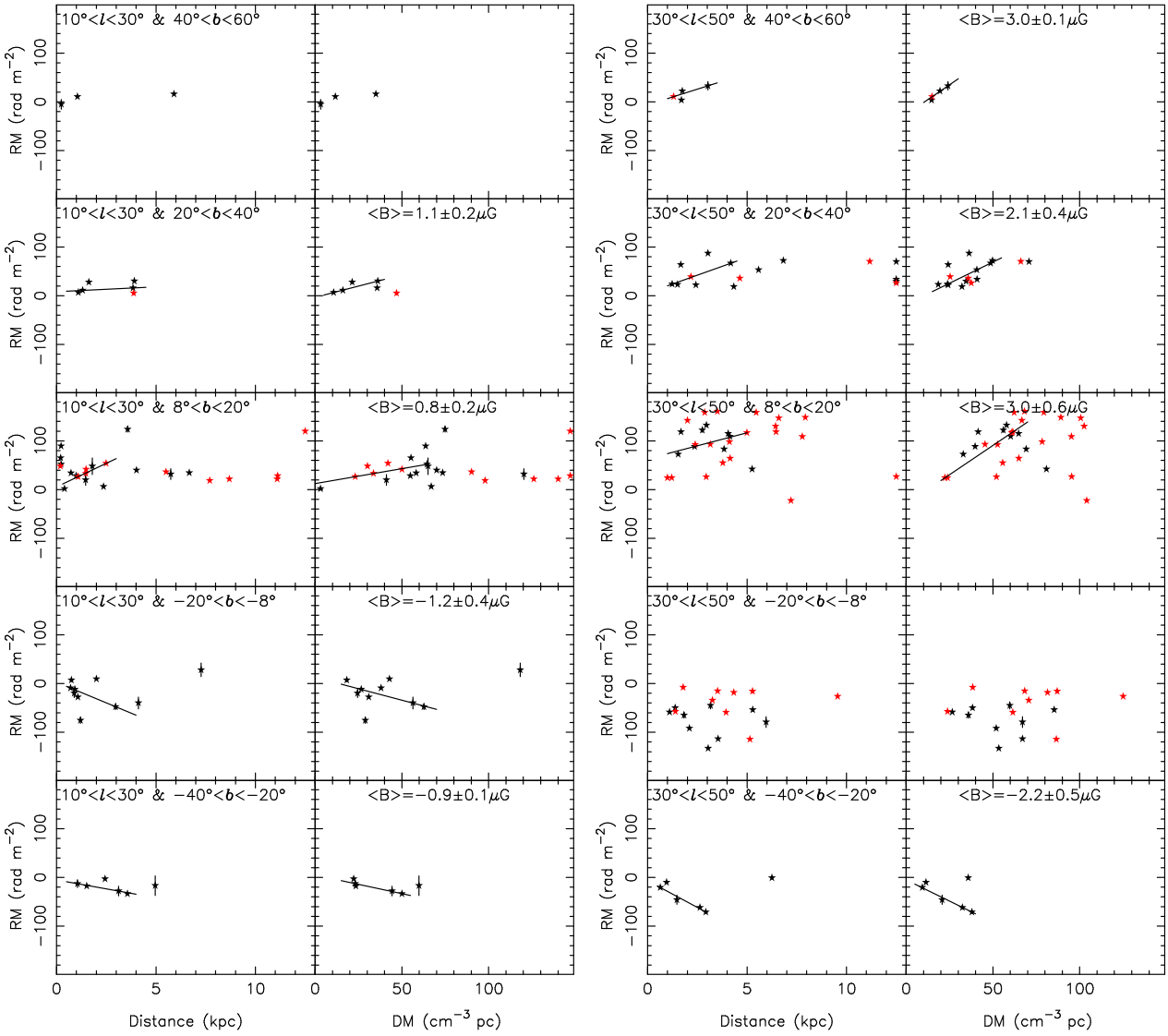


Figure 2 RMs (with error-bar) versus distance and DM for pulsars in the binned halo regions of the Galactic latitude of $8° < |b| < 60°$ and in the Galactic longitude ranges of $10° < l < 30°$ (*left*) and $30° < l < 50°$ (*right*). The red stars denote the newly obtained RMs for faint pulsars by FAST. The black lines represent the robust straight-line fitting (see §15.7 in Press et al., 1992) to RMs for pulsars. The mean line-of-sight magnetic field and its statistical uncertainty are given inside the panels, with positive slopes corresponding to mean fields towards us. The uncertainties of DMs are typically less than the symbol size and not plotted. The distance uncertainties for two thirds of pulsars are smaller than 20% (Yao et al., 2017).

3 Magnetic fields in the Galactic halo

Though the magnetic field structures in the Galactic halo have been qualitatively proposed by Han et al. (1997, 1999), and then quantitatively modelled by, e.g., Jansson & Farrar (2012); Prouza & Šmída (2003); Pshirkov et al. (2011); Sun et al. (2008); Terral & Ferrière (2017); Xu & Han (2019), many key parameters such as the scale radius, the scale height, the field strength and its variations as a function of radius and height, have not been well determined yet. There have been some efforts to analysis of pulsar RMs for the scale height of the Galactic halo fields (Sobey et al., 2019) and the field strength (Xu & Han, 2019). Based on much more pulsar data, we can investigate the nature of magnetic fields in the halo as follows.

3.1 The strength of magnetic fields in the Galactic halo

Since the RM distributions of pulsars and EGRS shows coherent structures on scales of several degrees to tens of degrees on the sky, if the halo fields are coherent on the large scales, the strength of magnetic fields can be estimated from the variations of pulsar RMs against DMs in a small sky area where pulsars are located in similar directions.

Considering the number density of pulsars, we divide the middle Galactic latitude region into a number of modest-

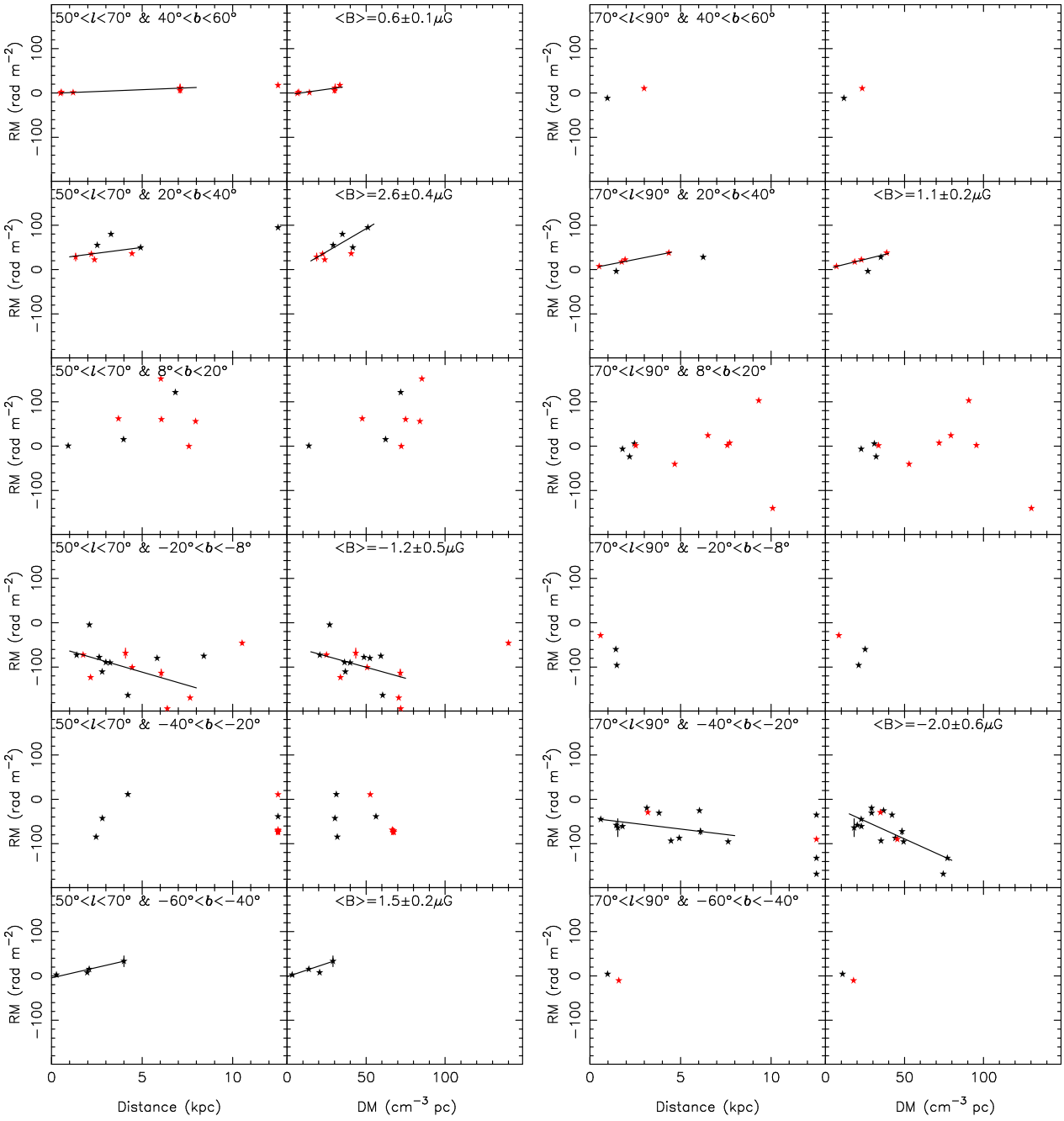


Figure 3 Same as Figure 2 but for RMs for pulsars in the binned halo regions of the Galactic longitude ranges $50^\circ < l < 70^\circ$ (*left*) and $70^\circ < l < 90^\circ$ (*right*).

sized bins to examine the RM trends over different distance intervals to pulsars. As shown in Figure 1, we make three Galactic latitude ranges for each hemisphere above and below the Galactic plane: $|b| = (8^\circ, 20^\circ)$, $(20^\circ, 40^\circ)$ and $(40^\circ, 60^\circ)$. Then each Galactic latitude range is further divided into six longitude ranges, four in the first quadrant from $l = 10^\circ$ to $l = 90^\circ$ with a width of 20° and two in the second quadrant from $l = 90^\circ$ to $l = 180^\circ$ with a width of 45°. The Galactic longitude ranges $l < 10^\circ$ excluded because the large-scale azimuthal fields become nearly perpendicular to the lines of sight close to the meridian through the Galactic Centre, and hence not easy to measure using Faraday rotation.

Since distances of individual pulsars determined from the Galactic electron density distribution models have unpredictable uncertainties and RMs of individual pulsars are subjected to small-scale fluctuations of the magnetic fields, following Han et al. (2006, 2018), we quantify the RM trends by fitting the variations of RM against DM and distance for groups of pulsars over some distance intervals where a significant correlation between RM and DM exists. To determine

the RM–DM slope, i.e., the averaged field strength along the line of sight, the Maximum Likelihood Robust Estimate routine (see §15.7 in Press et al., 1992) is used (i.e., the MEDFIT subroutine). The "robust" fitting is necessary to minimize the effects of outliers that could influence the slope of the fitted line resulting from un-modeled fluctuations of electron density and/or magnetic field along the path. A straight line is plotted in Figure 2, 3 and 4 for RMs over distance/DM ranges where the result is significant at least above 2-sigma of none-zero[6] The averaging over groups of pulsars will minimize the effects of distance uncertainties of individual pulsars. The uncertainty of the slope is taken as the mean absolute deviation of RMs from the fitted line divided by the DM range for the fitting. The scatter of data points around the fitted line reflects the random component of magnetic fields on the line of sight rather than the effects of small RM measurement uncertainties. Positive slopes of RM–DM denote magnetic fields with a direction towards us, while negative slopes denote fields pointing away from us. To improve the field estimates reliability, we have omitted the pulsar RMs with uncertainties larger than 30 rad m^{-2}.

We emphasize that the estimated magnetic fields are derived merely from the fits to RM versus DM. Figure 2 and 3 show pulsar RMs versus distance and DM in the halo areas towards the inner Galaxy, if there are more than 4 pulsars in the binned region, and Figure 4 show these relations towards the outer Galaxy. From the top sub-panels down, each shows RM relations in the regions from the northern hemisphere to the southern hemisphere. All derived values of magnetic field strength have more than or about 3-sigma significance of none-zero as listed in Table 4.

Towards the inner halo regions, as shown in Figure 2 and 3 and values for the longitude ranges $10° < l < 90°$ in Table 4, the estimated magnetic fields have positive values in the northern hemisphere and negative in the southern hemisphere, consistent with a bi-toroidal configuration of opposite field directions above and below the Galactic plane proposed by Han et al. (1997, 1999). The field strengths above and below the Galactic plane are roughly consistent with each other within the uncertainties, around 2 μG at $30° < l < 70°$. In most of the regions where the pulsar RM-DM data can be fitted (at least 2-sigma significance of non-zero), the far end of distance range for the fit is around 4–6 kpc. The RM data of pulsars have a larger dispersion at larger distances. The RM-DM data in some regions cannot be fitted due to either a small number of pulsars or a large scatter of RM values, but the RM tendency indicates a field as same as neighboring regions in the same hemisphere.

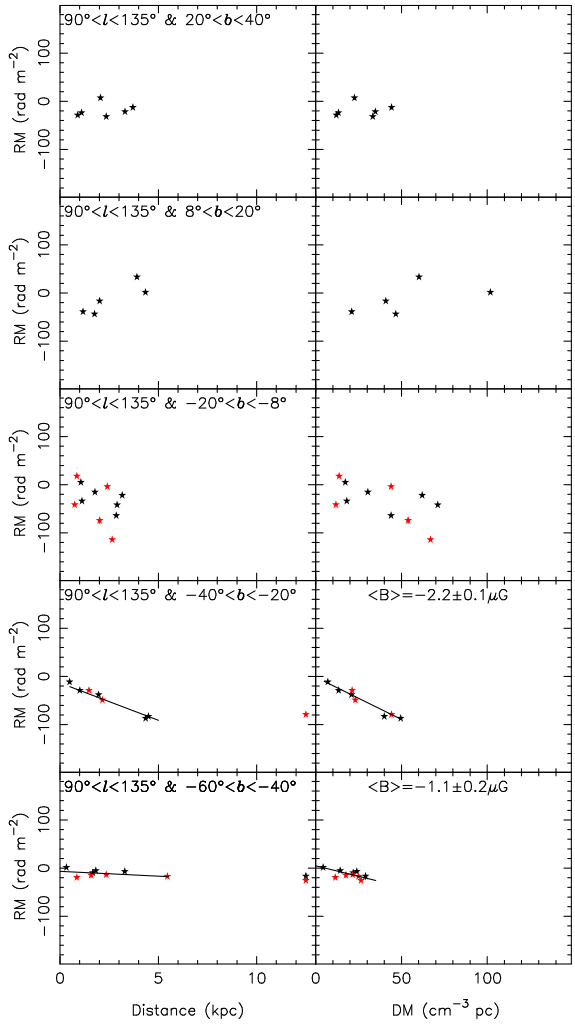


Figure 4 Same as Figure 2 but for RMs for pulsars in the binned halo regions of the Galactic longitude range $90° < l < 135°$.

Towards the outer Galactic halo, as shown in Figure 4, good RM-DM relations only exist in the southern hemisphere at $90° < l < 135°$. The maximum strength of line-of-sight component is up to around 2.2 μG, which indicates strong large-scale toroidal fields also exist in the south outer halo.

3.2 The scale height of the halo magnetic field

Early estimates of the scale height of the Galactic magnetic field are mainly based on RMs of EGRS. By assuming a uniform magnetic field model, Simard-Normandin & Kronberg (1980) estimate the full thickness of the magnetic disk of around 1.4 kpc by fitting the RM variance of EGRS in bins of

6) The straight line fitting over the DM range reflects a general trend which indicates the mean magnetic field. The scatter around the fitted line is mainly caused by the random magnetic field, rather than small measurement uncertainties. Therefore, the returned uncertainty of the fit represents the random magnetic field. Therefore, the 3-sigma criterion should not be a compulsory criterion if the random magnetic field is comparable to the large-scale mean magnetic field. For example, 0.5±0.2 μG is a good fitting, not necessary over 3σ.

10° in galactic latitude. Han & Qiao (1994) combine the uniform model of Simard-Normandin & Kronberg (1980) with variations of both field strength and electron density to estimate the scale height of about 1.2±0.4 kpc. The scale height would be much larger if a smaller electron density is adopted (Gaensler et al., 2008).

Table 4 Magnetic fields in the Galactic halo regions derived from pulsar DMs and RMs

b-range	D-range (kpc)	DM-range (cm^{-3} pc)	No. PSRs	$B_{\parallel}$ (μG)	B-field Direction
		$10° < l < 30°$			
(20°, 40°)	0.5–4.5	5–40	5	+1.1±0.2	ccw
(8°, 20°)	0.3–3.0	0–65	12	+0.8±0.2	ccw
(−20°, −8°)	0.5–4.0	15–70	9	-1.2±0.4	cw
(−40°, −20°)	0.5–4.0	15–55	5	-0.9±0.1	cw
		$30° < l < 50°$			
(40°, 60°)	1.0–3.5	10–30	4	+3.0±0.1	ccw
(20°, 40°)	1.0–4.5	15–55	14	+2.1±0.4	ccw
(8°, 20°)	1.0–5.0	20–70	20	+3.0±0.6	ccw
(−40°, −20°)	0.5–3.0	5–40	6	-2.2±0.5	cw
		$50° < l < 70°$			
(40°, 60°)	0.5–8	5–35	7	+0.6±0.1	ccw
(20°, 40°)	1–5	15–55	8	+2.6±0.4	ccw
(−20°, −8°)	1–8	15–75	16	-1.2±0.5	cw
(−60°, −40°)	0–4	0–30	4	+1.5±0.2	ccw
		$70° < l < 90°$			
(20°, 40°)	0.5–4.5	5–40	6	+1.1±0.2	ccw
(−40°, −20°)	0.5–8	15–80	17	-2.0±0.6	cw
		$90° < l < 135°$			
(−40°, −20°)	0.5–5	5–50	8	-2.2±0.1	cw
(−60°, −40°)	0–5.5	0–35	10	-1.1±0.2	cw

cw means clockwise, and ccw means counterclockwise.

Direct estimation of the parallel magnetic field along the sight lines decouples the scale heights for electron density and magnetic field. In comparison with the recent LOFAR survey (Sobey et al., 2019) and CHIME survey (Ng et al., 2020), our new measurements have largely increased the number of RMs for the distant pulsars in the first and second Galactic quadrant (see Figure 1). With the Z distribution of halo pulsars in a large range, the scale height of magnetic fields in the Galactic halo can be better constrained.

Figure 5 shows the averaged parallel magnetic field $\langle B_{\parallel}\rangle$ along the line of sight derived by using Equation (2) towards halo pulsars as a function of their vertical heights from the Galactic plane. Again, pulsars with RM uncertainties larger than 30 rad m^{-2} are discarded. Pulsars in Q1 indicate positive (negative) magnetic field values above (below) the Galactic plane, and most of those in Q2 have negative values. According to the data number distribution, we divide the data points into four Z-height ranges, $|Z|$ = (0.1, 0.8), (0.8, 1.5), (1.5, 3.0) and (3.0, 5.0) kpc. Referring to Sobey et al. (2019), the envelopes of $\langle B_{\parallel}\rangle$ distribution can be characterized by the "outermost" points, identified as the largest absolute values in the ranges. Exponential envelopes are clearly seen for magnetic fields at both positive and negative heights, as expressed by

$$\langle B_{\parallel}\rangle = \langle B_{\parallel}\rangle_0 \, exp(-|Z|/H), \tag{4}$$

where $\langle B_{\parallel}\rangle_0$ is the constant field value at $Z = 0$ and H is the scale height of magnetic fields. The magnetic scale heights derived in the areas of Q1+ and Q1- have a value of 2.7~3.0 kpc. The scale height in the Q2- area has a value of 3.7 kpc but with large uncertainty. In contrast, the Q2+ area has a much smaller scale height, only 0.8 kpc. The large scale heights in the three areas of Q1+, Q1-, and Q2- are also supported by distant pulsars with vertical height beyond 6 kpc, as seen in the figure, though distances of those distant pulsars are likely overestimated. The fits to all pulsar data for the three areas of Q1&Q2- gives a value of 2.7±0.3 kpc, slightly larger than the scale height of 2.0 kpc estimated by Sobey et al. (2019). Note that this derived value of 2.7 kpc is the

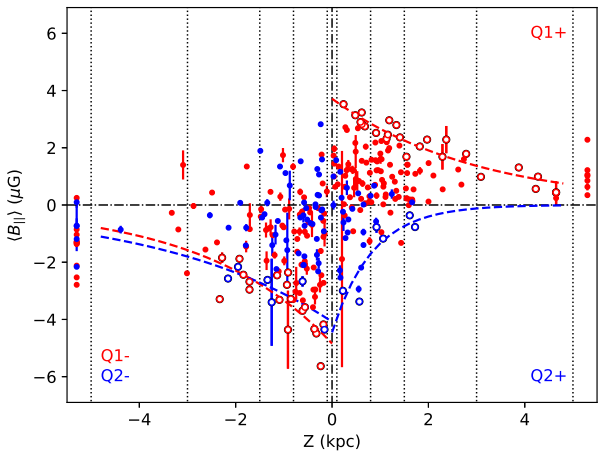


Figure 5 The parallel magnetic fields along the sight-line path as a function of vertical height above/below the Galactic plane for the halo pulsars of $|b| > 8°$ located in the first Galactic quadrant (Q1: $10° < l < 90°$) and the second quadrant (Q2: $90° < l < 180°$). The vertical dotted lines indicate the height at $|Z|$ = 0.1, 0.8, 1.5, 3.0 and 5.0 kpc. Pulsars with heights beyond 6 kpc are plotted at $|Z|$ = 5.3 kpc. Red points represent pulsars in Q1, and blue points in Q2. The "outermost" points in the four areas labeled Q1+, Q1-, Q2+ and Q2- are indicated by open circles. Dashed lines outline fitting results to the "outermost" data points.

4 Magnetic fields in the first quadrant of the Galactic disk

The GPPS survey has discovered more than 500 new pulsars in the Galactic disk of $|b| < 10°$, and redetected most of previously known pulsars in the survey region (Han et al., 2021). Polarization data are recorded for most of the pulsars during the survey observation. In the FAST pulsar database of

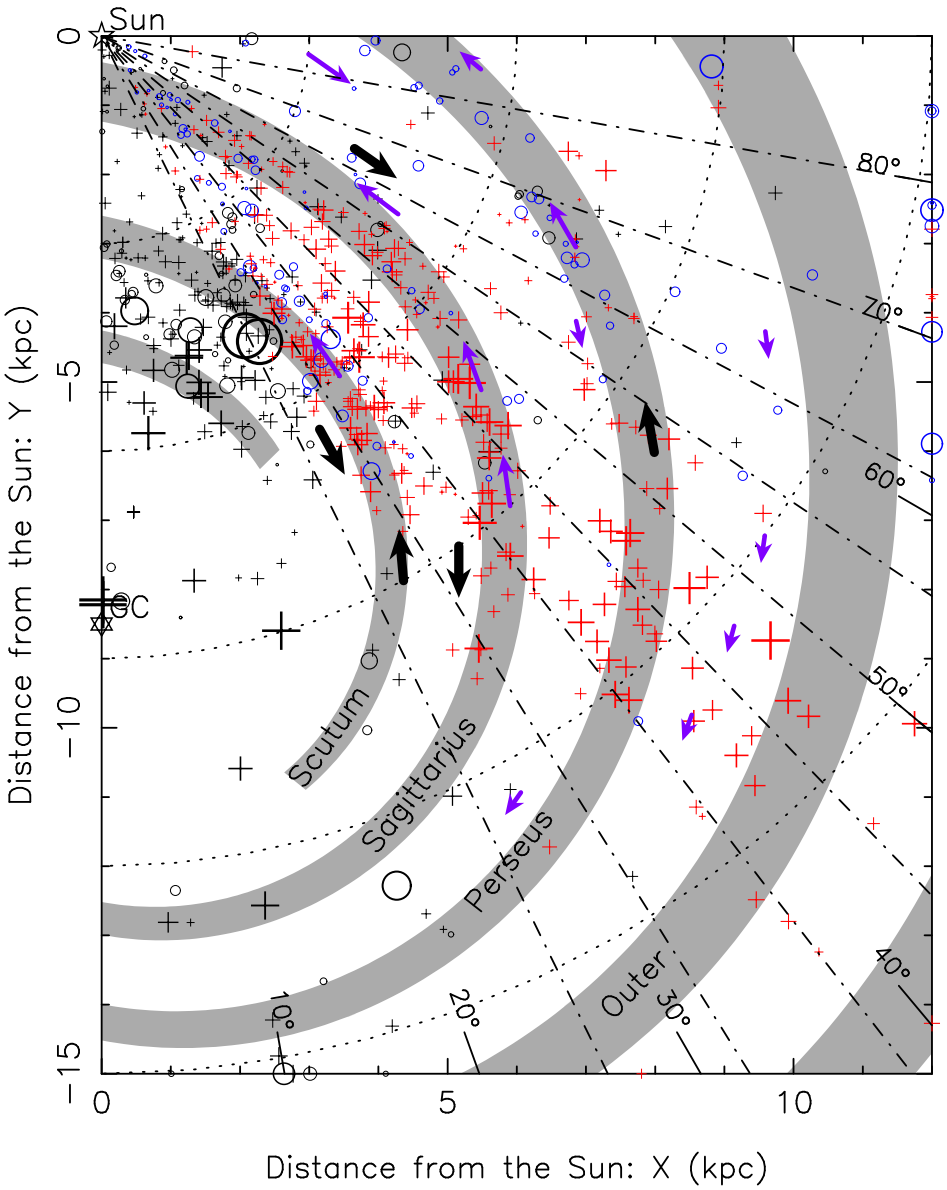


Figure 6 RM distribution of pulsars of $|b| < 8°$ in the first Galactic quadrant. The symbols are as same as in Figure 1. New measurements are indicated by red crosses and blue circles for positive and negative values. The approximate locations of spiral arms (see Hou & Han, 2014) are indicated in shadow. The dot-dashed lines give the longitude boundaries for the RM analyses in this paper. Distances to pulsars are estimated by using the YMW16 Galactic electron density distribution model (Yao et al., 2017). Two thirds of them have an uncertainty less than 20%. Pulsars with distances too large to show in the plot ranges are plotted at the boundaries. Magnetic field directions inferred from RM-DM fits (at least 2-sigma significance of non-zero) of pulsars are plotted with thick long arrows representing new determinations and with thin arrows for previously known directions. Short arrows give a inferred direction derived from the RM comparison of EGRS and most distant pulsars.

Wang et al. (2022), we determined RMs for the newly discovered pulsars and many known pulsars (including 134 RMs of halo pulsars in this work). Among them, RMs of 311 pulsars are first time measured, and RMs of 161 pulsars are updated. This large number of RMs for weak distant pulsars in the Galactic longitude of $26° < l < 90°$ in the first quadrant (see Figure 6) increased by a factor of more than two compared to the previous work in the longitude ranges (Han et al., 2018). This has enabled us to explore the magnetic fields in farther arms up to 15 kpc in the first Galactic quadrant.

Han et al. (2018) have shown counterclockwise magnetic fields in spiral arms from pulsars with positive RMs and reversed field directions in interarm regions inferred from distant pulsars and EGRS. However, magnetic fields beyond the tangential region of spiral arms are not well constrained yet. We make quantitative analysis of RM variation against DM and distance for pulsars in the first quadrant following Han et al. (2018). Similar to the halo pulsars, we make the robust straight-line fitting (see §15.7 in Press et al., 1992) to RMs against distance over specified distance intervals and RM

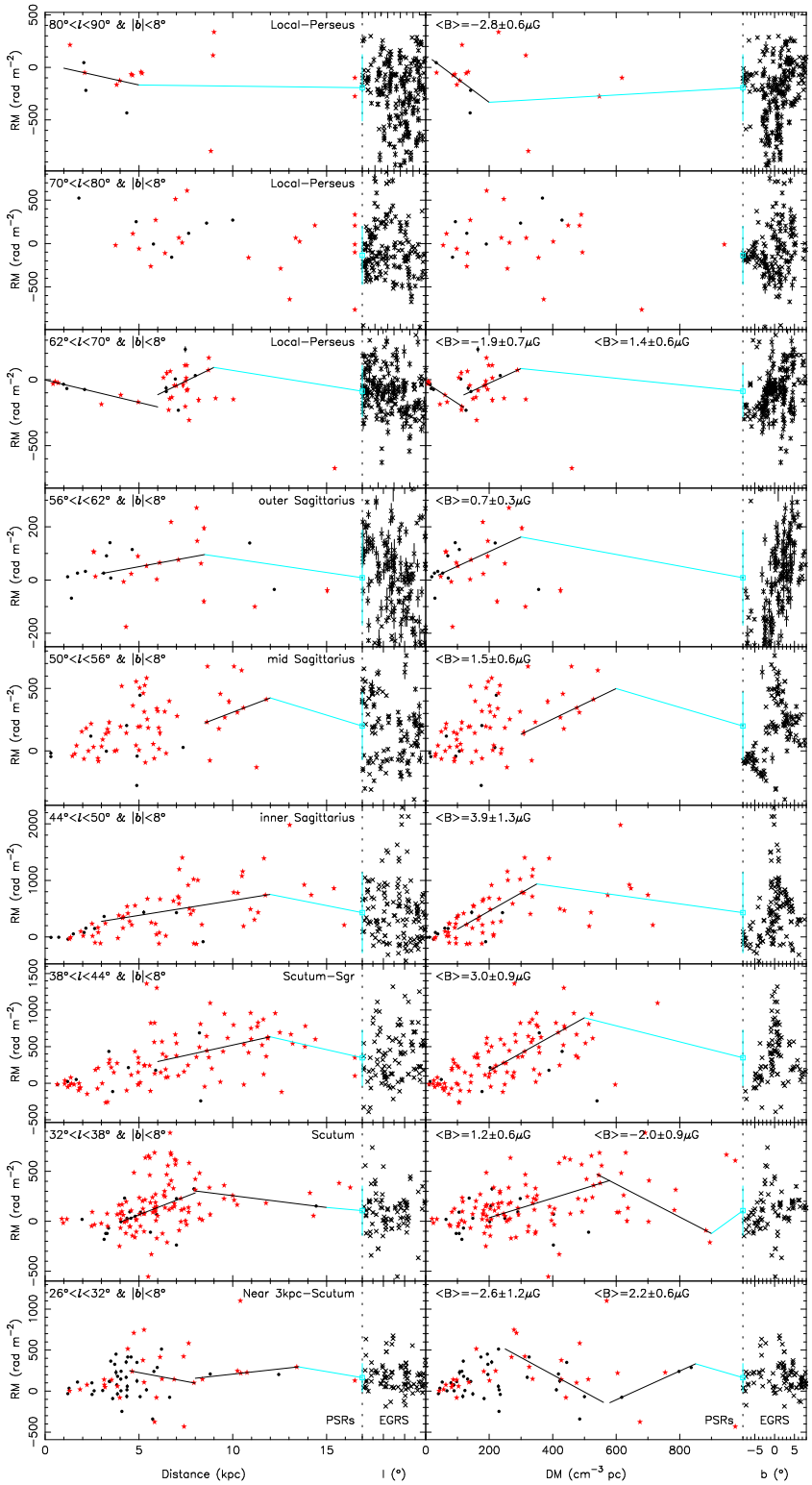


Figure 7 RMs for pulsars versus distance and DM, and RMs for EGRS versus the Galactic longitude (scale ticks are given but not labeled) and the Galactic latitude in several longitude intervals at $26^\circ < l < 90^\circ$ of the Galactic disk. The red stars denote the newly obtained RMs by the FAST, and the black dots represent previously known RMs. The black lines represent the robust straight-line fitting (see §15.7 in Press et al., 1992) to RMs for pulsars. The blue lines indicate the comparison of RMs of the most distant pulsars to the median of the EGRS RMs that are denoted by the blue squares with error bars representing the standard deviation from the median in the region. The EGRS RMs are collected from the literature (Brown et al., 2003; Clegg et al., 1992; Lazio et al., 1990; Ma et al., 2020; Schnitzeler et al., 2019; Shanahan et al., 2019; Taylor et al., 2009; Van Eck et al., 2011, 2021).

Table 5 Magnetic fields in the first Galactic quadrant

Region	l-range (°)	D-range (kpc)	DM-range (cm^{-3} pc)	No. PSRs or EGRS	$B_{\parallel}$ (μG)	B-field Direction	Arrow l (°)	Arrow D (kpc)
Near 3-kpc–Scutum_1	$26° < l < 32°$	4.5–8.0	250–560	21	-2.6±1.2	cw	29	6.5
Near 3-kpc–Scutum_2	$26° < l < 32°$	8.0–13.5	580–850	6	2.2±0.6	ccw	29	9.0
Near 3-kpc–Scutum–EGRS	$26° < l < 32°$	13.5–E	850–E	92	–	cw	29	12.5
Scutum_1	$32° < l < 38°$	4.0–8.0	200–580	73	1.2±0.6	ccw	35	6.0
Scutum_2	$32° < l < 38°$	8.0–15.0	540–900	19	-2.0±0.9	cw	35	9.0
Scutum–EGRS	$32° < l < 38°$	15.0–E	900–E	87	–	–	–	–
Scutum-Sgr	$38° < l < 44°$	6.0–12.0	200–500	52	3.0±0.9	ccw	41	9.0
Scutum-Sgr–EGRS	$38° < l < 44°$	12.0–E	500–E	105	–	cw	41	13.0
inner Sagittarius	$44° < l < 50°$	3.0–12.0	100–350	38	3.9±1.3	ccw	47	7.5
inner Sagittarius–EGRS	$44° < l < 50°$	12.0–E	350–E	148	–	cw	47	12.5
mid Sagittarius	$50° < l < 56°$	8.5–12.0	300–600	13	1.5±0.6	ccw	53	10.0
mid Sagittarius–EGRS	$50° < l < 56°$	12.0–E	600–E	126	–	cw	53	12.0
outer Sagittarius	$56° < l < 62°$	3.0–8.5	40–300	22	0.7±0.3	ccw	59	5.0
outer Sagittarius–EGRS	$56° < l < 62°$	8.5–E	300–E	184	–	cw	59	8.0
Local-Perseus_1	$62° < l < 70°$	0–6.0	0–120	14	-1.9±0.7	cw	66	4.0
Local-Perseus_2	$62° < l < 70°$	6.0–9.0	120–300	22	1.4±0.6	ccw	66	7.5
Local-Perseus–EGRS	$62° < l < 70°$	9.0–E	300–E	232	–	cw	66	10.5
Local-Perseus	$70° < l < 80°$	–	–	–	–	–	–	–
Local-Perseus–EGRS	$70° < l < 80°$	–	–	–	–	–	–	–
Local-Perseus	$80° < l < 90°$	1.0–5.0	20–200	11	-2.8±0.6	cw	85	3.0
Local-Perseus–EGRS	$80° < l < 90°$	5.0–E	200–E	244	–	ccw	85	5.5

cw means clockwise and ccw means counterclockwise. The field direction obtained by arm to EGRS is indicative and inferred from RMs of the most distant pulsars and the median RM of EGRS.

against DM in DM ranges which match the distance range as closely as possible. The longitude intervals are divided equally with a width of 6° at $26° < l < 62°$ but a bit wider at $l > 62°$ due to sparse data at larger longitudes. The specified distance intervals for each longitude range are guided by arm/interarm zones characterized by the spiral model of Hou & Han (2014). Again, pulsar RMs with uncertainties larger than 30 rad m^{-2} are omitted. The regions for which we have analyzed the RMs are listed in Table 5.

We derive the magnetic field directions from the RM trends beyond the tangential regions of spiral arms that have not been detected before (see Figure 6). Although distances to individual pulsars may be subject to some unpredictable uncertainties, the RM distribution trends versus distance or DM for a group of pulsars can indicate magnetic fields in the range. The pulsar RMs as functions of distance and DM of the regions are presented in Figure 7. The derived field directions are illustrated in Figure 6. Locations of direction arrows at the mean longitude and the approximate mean distance for the relevant RM-DM fit are listed in Table 5.

Inside the Sagittarius arm, spiral arms are tightly enwinded. Previously, the magnetic fields in the Norma arm, the Crux-Scutum arm and the Carina-Sagittarius arm conform to the counterclockwise pattern both in the first and fourth quadrant (Han et al., 2006, 2018; Noutsos et al., 2008). Evidence for clockwise fields in interarm regions is demonstrated in the fourth quadrant (Han et al., 2006, 2018; Nota & Katgert, 2010). The clockwise field near or beyond the Scutum arm was suggested by Rand & Lyne (1994) based on negative pulsars RMs, and supported by variation of EGRS RMs behind the Galactic disk (e.g. Van Eck et al., 2011). The careful analysis gives only weak evidence for clockwise fields in the Scutum-Sagittarius interarm, mainly based on the RM difference between distant pulsars and EGRS (Han et al., 2018).

Figure 7 shows positive RMs decreasing with distance and DM in the Near 3kpc-Scutum interarm tangential region ($26° < l < 32°$) between 4.5 kpc and 8 kpc, conforming to the clockwise magnetic fields in the Crux-Norma interarm region previously determined in the fourth quadrant (Han et al., 2018). Beyond the interarm region, a positive slope of more distant pulsars ($D > 8$ kpc) indicates a counterclockwise field that could result from the Scutum arm. Comparison of RMs for most distant pulsars with EGRS RMs may show another reverse farther than these pulsars, though it is not possible to determine exactly where the reversal occurs. Because both the magnetic field strength and the electron density generally decline as the Galactocentric radius increases, it is reasonable to assume the reversal happens in the next arm/interarm region.

In the Scutum tangential region ($32° < l < 38°$) between 4 kpc and 8 kpc, the increase of RM with distance and DM provides evidence for counterclockwise fields in this region, which is already obtained by Han et al. (2018). The decreasing RM-DM relation beyond the tangential zone based on the newly determined pulsar RMs at $D > 8$ kpc clearly shows a reversed field in the Scutum-Sgr interarm region or beyond.

Pulsar RMs in the longitude intervals from $38° < l < 62°$ further show evidence for counterclockwise pattern in dif-

ferent sections of Sagittarius arm and Perseus arm (farther part beyond the tangential regions of these arms), and possible field reversals between the end of fitting regions and the edge of the Galaxy by comparing RMs of distant pulsars and EGRS RMs.

The clockwise magnetic field in the Local interarm within 3 kpc between the Sagittarius arm and Perseus arm has long been known (e.g. Manchester, 1974) based on primarily negative pulsar RMs within 30° of $l = 90°$ and mostly positive RMs in the opposite direction. The field direction in the Local-Perseus interarm beyond 3 kpc was not known due to insufficient pulsar data nearer than 6 kpc in the direction of $60° < l < 90°$. The fields here also cannot be constrained by EGRS RMs behind the disk (Van Eck et al., 2011). Han et al. (2018) show clear evidence for counterclockwise fields in the Perseus arm presented by the increasing RM pattern for pulsars at $D > 5$ kpc in the range of $60° < l < 80°$. They also show weak evidence for another field reversal beyond the Perseus arm based on smaller RMs of EGRS in this direction. Based on primarily new RM data from the FAST, as shown in Figure 7, RMs decrease nearer than 6 kpc in the longitude interval $62° < l < 70°$ and then RM values become positive for distant pulsars beyond 6 kpc. It implies a clockwise field in the Local-Perseus interarm region and a reversal occurs in the Perseus arm. The counterclockwise field in the Perseus arm is echoed by the neighboring longitude interval $70° < l < 80°$ where a possible positive slope of RM-Distance relation is found for pulsars between 5 kpc and 9 kpc. Beyond the fitting region in the two longitude intervals, there seems to be another field reversal exterior to the Perseus arm indicated by smaller RMs of distant pulsars and EGRS RMs. Pulsar RMs in the longitude range $80° < l < 90°$ also support the clockwise field in the Local-Perseus interarm region.

5 Conclusions

Observations of Faraday rotation of a large number of pulsars inside the Milky Way give key probes to reveal the large-scale Galactic magnetic field structure. The super sensitivity of the FAST enables us to not only discover faint pulsars but also measure their polarization and hence the RMs, which were not possible before by using other radio telescopes. The obtained RMs enable us to explore the feature of the Galactic magnetic fields in much wide regions.

We have measured rotation measures for 134 weak pulsars in the Galactic halo using the FAST, most located in the first Galactic quadrant. The basic parameters for 15 pulsars including positions and period are also improved. Together with many newly determined RMs for newly-discovered pulsars and faint pulsars, and also newly measured RMs for a large number of the known pulsars, we make tomographic analysis of the magnetic field structure both in the Galactic halo and the Galactic disk.

By analyzing the pulsar RM variations against pulsar distance and DM within a number of regions in the Galactic halo, we confirm the halo toroidal fields with opposite directions above and below the Galactic plane and determine the field strength of around 2 μG. The scale height of halo fields is estimated to be at least 2.7±0.3 kpc.

Tomographic analysis for pulsar RMs in the Galactic longitude range of $26° < l < 90°$ gives evidence for the clockwise magnetic fields in two interarm regions interior to the Scutum arm and between the Scutum and the Sagittarius arm, respectively. We confirm the counterclockwise field pattern in the Sagittarius arm and Perseus arm. The clockwise field direction in the Local-Perseus interarm region and field reversals in the Perseus arm and beyond are also well revealed by newly observed pulsar RMs by the FAST.

Acknowledgements. This work is supported by the National Natural Science Foundation of China (Grant Nos. 11988101, 11833009, and U2031115), the Key Research Program of the Chinese Academy of Sciences (Grant No. QYZDJSSW- SLH021), and the National SKA Program of China (Grant No. 2022SKA0120103). Pengfei Wang was supported by the National Natural Science Foundation of China (Grant No. 11873058 and 12133004), and the National SKA Program of China (Grant No. 2020SKA0120200). We thank Prof. R.T. Gangadhara for careful English corrections. The GPPS survey is one of the five key projects carried out by FAST, which is a Chinese national mega-science facility built and operated by the National Astronomical Observatories, Chinese Academy of Sciences.

References

Beck, R., Shukurov, A., Sokoloff, D., & Wielebinski, R. 2003, AAP, 411, 99

Bennett, C. L., Larson, D., Weiland, J. L., et al. 2013, ApJS, 208, 20

Beuermann, K., Kanbach, G., & Berkhuijsen, E. M. 1985, AAP, 153, 17

Bilous, A. V., Kondratiev, V. I., Kramer, M., et al. 2016, AAP, 591, A134

Brown, J. C., Haverkorn, M., Gaensler, B. M., et al. 2007, ApJ, 663, 258

Brown, J. C., Taylor, A. R., & Jackel, B. J. 2003, ApJS, 145, 213

Chi, X., & Wolfendale, A. W. 1990, Journal of Physics G Nuclear Physics, 16, 1409

Clegg, A. W., Cordes, J. M., Simonetti, J. M., & Kulkarni, S. R. 1992, ApJ, 386, 143

Clemens, D. P., Pinnick, A. F., Pavel, M. D., & Taylor, B. W. 2012, ApJS, 200, 19

Crutcher, R. M. 2012, ARA&A, 50, 29

Crutcher, R. M., Wandelt, B., Heiles, C., Falgarone, E., & Troland, T. H. 2010, ApJ, 725, 466

Deneva, J. S., Stovall, K., McLaughlin, M. A., et al. 2013, ApJ, 775, 51

Deneva, J. S., Stovall, K., McLaughlin, M. A., et al. 2016, ApJ, 821, 10

Edwards, R. T., Bailes, M., van Straten, W., & Britton, M. C. 2001, MNRAS, 326, 358

Gaensler, B. M., Madsen, G. J., Chatterjee, S., & Mao, S. A. 2008, PASA, 25, 184

Gao, X. Y., Reich, W., Sun, X. H., et al. 2022, SCPMA, 65, 129705

Han, J. L. 2017, ARA&A, 55, 111

Han, J. L., Manchester, R. N., Berkhuijsen, E. M., & Beck, R. 1997, A&A, 322, 98

Han, J. L., Manchester, R. N., Lyne, A. G., & Qiao, G. J. 2002, ApJ, 570, L17

Han, J. L., Manchester, R. N., Lyne, A. G., Qiao, G. J., & van Straten, W. 2006, ApJ, 642, 868

Han, J. L., Manchester, R. N., & Qiao, G. J. 1999, MNRAS, 306, 371

Han, J. L., Manchester, R. N., van Straten, W., & Demorest, P. 2018, ApJS, 234, 11

Han, J. L., & Qiao, G. J. 1994, AAP, 288, 759

Han, J. L., Wang, C., Wang, P. F., et al. 2021, Research in Astronomy and Astrophysics, 21, 107

Heiles, C. 1996, ApJ, 462, 316

Hong, T., Han, J. L., Hou, L. G., et al. 2022, SCPMA, 65, 129702

Hotan, A. W., van Straten, W., & Manchester, R. N. 2004, PASA, 21, 302

Hou, L. G., & Han, J. L. 2014, AAP, 569, A125

Hou, L. G., Han, J. L., Hong, T., Gao, X. Y., & Wang, C. 2022, SCPMA, 65, 129703

Hutschenreuter, S., Anderson, C. S., Betti, S., et al. 2022, AAP, 657, A43

Indrani, C., & Deshpande, A. A. 1999, New Ast., 4, 33

Jansson, R., & Farrar, G. R. 2012, ApJ, 757, 14

Jiang, P., Yue, Y., Gan, H., et al. 2019, Science China Physics, Mechanics, and Astronomy, 62, 959502

Lazio, T. J., Spangler, S. R., & Cordes, J. M. 1990, ApJ, 363, 515

Letessier-Selvon, A., & Stanev, T. 2011, Reviews of Modern Physics, 83, 907

Lommen, A. N., Zepka, A., Backer, D. C., et al. 2000, ApJ, 545, 1007

Lyne, A. G., & Smith, F. G. 1989, MNRAS, 237, 533

Ma, Y. K., Mao, S. A., Ordog, A., & Brown, J. C. 2020, MNRAS, 497, 3097

Manchester, R. N. 1974, ApJ, 188, 637

Manchester, R. N., Hobbs, G. B., Teoh, A., & Hobbs, M. 2005, AJ, 129, 1993

Mao, S. A., Gaensler, B. M., Haverkorn, M., et al. 2010, ApJ, 714, 1170

Mao, S. A., McClure-Griffiths, N. M., Gaensler, B. M., et al. 2012, ApJ, 755, 21

Men, H., Ferrière, K., & Han, J. L. 2008, AAP, 486, 819

Nan, R. 2008, in Society of Photo-Optical Instrumentation Engineers (SPIE) Conference Series, Vol. 7012, Ground-based and Airborne Telescopes II, ed. L. M. Stepp & R. Gilmozzi, 70121E

Nan, R., Li, D., Jin, C., et al. 2011, International Journal of Modern Physics D, 20, 989

Ng, C., Pandhi, A., Naidu, A., et al. 2020, MNRAS, 496, 2836

Nota, T., & Katgert, P. 2010, AAP, 513, A65

Noutsos, A., Johnston, S., Kramer, M., & Karastergiou, A. 2008, MNRAS, 386, 1881

Oppermann, N., Junklewitz, H., Robbers, G., et al. 2012, AAP, 542, A93

Oppermann, N., Junklewitz, H., Greiner, M., et al. 2015, AAP, 575, A118

Ordog, A., Brown, J. C., Kothes, R., & Landecker, T. L. 2017, AAP, 603, A15

Planck Collaboration, Adam, R., Ade, P. A. R., et al. 2016a, AAP, 594, A1

Planck Collaboration, Adam, R., Ade, P. A. R., et al. 2016b, AAP, 596, A103

Press, W. H., Teukolsky, S. A., Vetterling, W. T., & Flannery, B. P. 1992, Numerical Recipes: The Art of Scientific Computing, 2^{nd} edition (Cambridge: Cambridge University Press)

Prouza, M., & Šmída, R. 2003, AAP, 410, 1

Pshirkov, M. S., Tinyakov, P. G., Kronberg, P. P., & Newton-McGee, K. J. 2011, ApJ, 738, 192

Rand, R. J., & Kulkarni, S. R. 1989, ApJ, 343, 760

Rand, R. J., & Lyne, A. G. 1994, MNRAS, 268, 497

Sanidas, S., Cooper, S., Bassa, C. G., et al. 2019, AAP, 626, A104

Schnitzeler, D. H. F. M., Carretti, E., Wieringa, M. H., et al. 2019, MNRAS, 485, 1293

Seta, A., & Federrath, C. 2021, MNRAS, 502, 2220

Shanahan, R., Lemmer, S. J., Stil, J. M., et al. 2019, ApJ, 887, L7

Simard-Normandin, M., & Kronberg, P. P. 1980, ApJ, 242, 74

Sobey, C., Bilous, A. V., Grießmeier, J.-M., et al. 2019, MNRAS, 484, 3646

Sotomayor-Beltran, C., Sobey, C., Hessels, J. W. T., et al. 2013, ionFR: Ionospheric Faraday rotation, Astrophysics Source Code Library, record ascl:1303.022

Spiewak, R., Bailes, M., Miles, M. T., et al. 2022, arXiv e-prints, arXiv:2204.04115

Sun, X. H., Reich, W., Waelkens, A., & Enßlin, T. A. 2008, AAP, 477, 573

Taylor, A. R., Stil, J. M., & Sunstrum, C. 2009, ApJ, 702, 1230

Terral, P., & Ferrière, K. 2017, AAP, 600, A29

Thomson, R. C., & Nelson, A. H. 1980, MNRAS, 191, 863

Tyul'bashev, S. A., Tyul'bashev, V. S., Oreshko, V. V., & Logvinenko, S. V. 2016, Astronomy Reports, 60, 220

Tyul'bashev, S. A., Tyul'bashev, V. S., Kitaeva, M. A., et al. 2017, Astronomy Reports, 61, 848

Vallee, J. P. 1991, ApJ, 366, 450

Vallée, J. P. 2005, ApJ, 619, 297

Van Eck, C. L., Brown, J. C., Stil, J. M., et al. 2011, ApJ, 728, 97

Van Eck, C. L., Brown, J. C., Ordog, A., et al. 2021, ApJS, 253, 48

van Straten, W., & Bailes, M. 2011, PASA, 28, 1

Wahl, H. M., McLaughlin, M. A., Gentile, P. A., et al. 2022, ApJ, 926, 168

Wang, C., Han, J. L., & Lai, D. 2011, MNRAS, 417, 1183

Wang, P. F., Han, J. L., Xu, J., et al. 2022, RAA, Submitted

Wu, Q., Kim, J., & Ryu, D. 2015, New Ast., 34, 21

Wu, Q., Kim, J., Ryu, D., Cho, J., & Alexander, P. 2009, ApJ, 705, L86

Xiao, M., Perez, K. M., Giannotti, M., et al. 2021, Phys. Rev. Lett., 126, 031101

Xu, J., & Han, J.-L. 2014, Research in Astronomy and Astrophysics, 14, 942

Xu, J., & Han, J. L. 2019, MNRAS, 486, 4275

Yao, J. M., Manchester, R. N., & Wang, N. 2017, ApJ, 835, 29